Electronic Supplementary Information (ESI)

Significantly Improved Li-Ion Diffusion Kinetics and Reversibility of Li_2O in MoO_2 Anode: the Effects of Oxygen Vacancy-Induced Local Charge Distribution and Metal Catalysis on Lithium Storage

Tao Meng[a], Jinwen Qin[a], Zhen Yang[a], Lirong Zheng[b], and Minhua Cao[a,*]

[a]Key Laboratory of Cluster Science, Ministry of Education of China, Beijing Key Laboratory of Photoelectronic/Electrophotonic Conversion Materials, School of Chemistry and Chemical Engineering, Beijing Institute of Technology, Beijing 100081, P. R. China.

[b]Beijing Synchrotron Radiation Laboratory, Institute of High Energy Physics, Chinese Academy of Sciences, Beijing 100049, P. R. China.

* E-mail: caomh@bit.edu.cn

1 Characterizations

Powder X-ray diffraction (XRD) analysis was performed on a Bruker D8 Advance diffractometer (Cu-Kα, λ ≈ 0.154). Field emission scanning electron microscopy (FE-SEM) and transmission electron microscopy (TEM) measurements were performed on HITACHI S-4800 and JEOL JEM-2010 microscope, respectively. Energy dispersive spectroscopy (EDS) element mapping images were taken on TEM. Thermogravimetric analysis (TGA) was performed on a Rigaku thermogravimetry (TG) analyser in air. Raman spectra were collected on an Invia Raman spectrometer with the excitation laser wavelength of 633 nm. The Belsorp-max sorption analyzer was used to collect the N_2 adsorption-desorption isotherms at liquid nitrogen temperature (77 K). Before measurement, the sample was degassed at 200 °C for 3 h. Surface area was calculated by the multi-point Brunauer-Emmett-Teller (BET) method. The pore-size distribution was calculated from the adsorption branch using the Barrett-Joyner-Halenda (BJH) method. X-ray spectroscopy (XPS) was performed on the ESCALAB 250 sepctrometer (Perkin-Elmer). The Jobin Yvon Fluorolog 3-TAU luminescence spectrometer with a 450-W Xe lamp was employed to obtain the photoluminescence (PL) spectra. Room-temperature electron spin resonance (ESR) spectra were obtained using a JEOL JES-FA200 ESR spectrometer (300 K, 9.062 GHz). The content of molybdenum element was determined by inductively coupled plasma mass spectroscopy (ICP-MS) analysis (Thermo Fisher Scientific, U.S.). The X-ray absorption near edge structure (XANES) measurement was undertaken at Beamlines 1W1B at Beijing Synchrotron Radiation Facility (BSRF) using transmission modes.

2. Lithium-ion battery measurements

To prepare the working electrode for LIBs, the as-obtained material, acetylene black, and sodium carboxymethyl cellulose binder (CMC) with a mass ratio of 8:1:1 were firstly mixed together by trace water to form a homogeneous slurry, which then was coated onto Cu foil and dried at 120 °C for 36 h in vacuum oven. The mass loading of each as-prepared working electrode was around 1 mg. The cell [coin cells (CR2025)] assembly was operated in an Ar-filled glovebox. The Celgard 2400 microporous

polypropylene membrane and Li foil were used as the separator and the counter electrode, respectively. The non-aqueous electrolyte used was 1 M $LiPF_6$ dissolved in ethylene carbonate (EC)/dimethyl carbonate (DMC)/diethyl carbonate (DEC) mixture (1:1:1, in vol. %). The cyclic voltammetry (CV) tests were carried out at scan rates ranging from 0.1 to 3 mV s^{-1} on a CHI-760E workstation. Galvanostatic cycling experiments of the cell were performed on a LAND CT2001A cell at different current densities in the voltage range of 0.01-3.00 V *vs.* Li^+/Li at room temperature. Electrochemical impedance spectroscopy (EIS) measurements were recorded in a frequency range of 100,000 to 0.01 Hz with AC oscillation of 5 mV at the open circuit voltage.

3. Supplementary figures

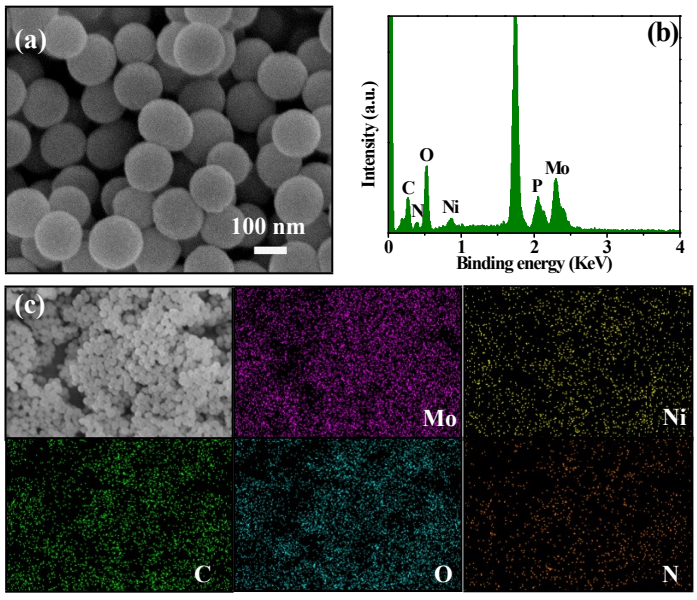

Fig. S1 (a) FESEM image, (b) energy-dispersive spectroscopy (EDS) spectrum and (c) corresponding element mappings over a widespread region of Ni,Mo-precursor.

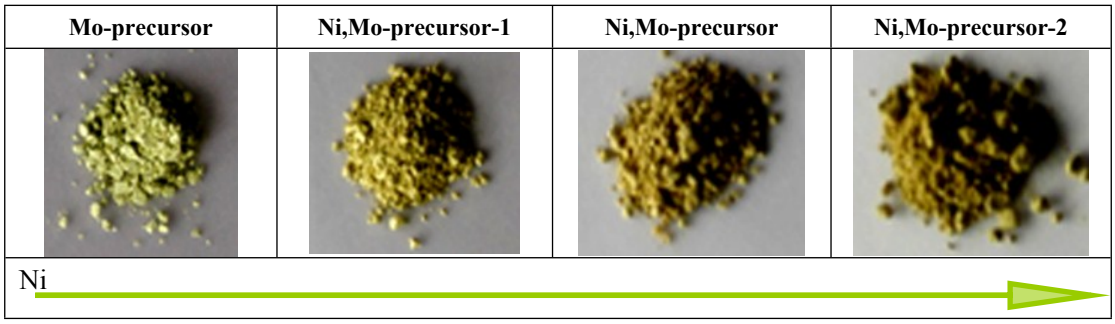

Fig. S2 Digital photographs of Ni,Mo-precursor with different Ni species, and corresponding color change of the products.

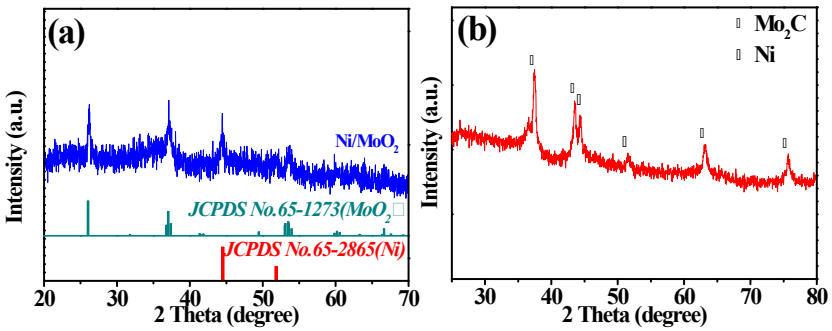

Fig. S3 XRD patterns of (a) Ni/MoO_2 and (b) Ni/Mo_2C.

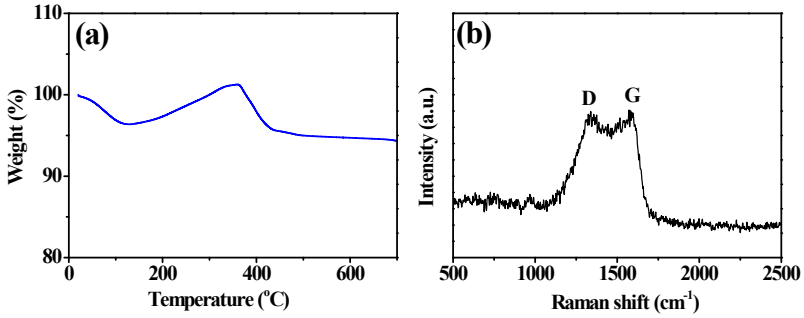

Fig. S4 TGA curve (a) and Raman spectrum (b) for $Ni/MoO_{2-\delta}$

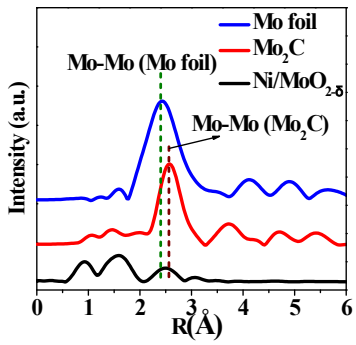

Fig. S5 Fourier transform k^3-weighted EXAFS spectra of Ni/$MoO_{2-\delta}$, Mo_2C and Mo foil.

The R space of 1.55 Å for Ni/$MoO_{2-\delta}$ corresponds to the Mo-O bond, which is also similar with that of MoO_2. The weak peak at the R space of 2.51 Å in Ni/$MoO_{2-\delta}$ can be ascribed to the Mo-Mo bond in Mo_2C species (Fig. S5). From this result we also deduce that a little Mo_2C has been formed existing in Ni/$MoO_{2-\delta}$ sample during the heat treatment process. In fact, $MoO_{2-\delta}$ can be completely transformed into Mo_2C by prolonging the annealing time (Fig. 1h and Fig. S3b).

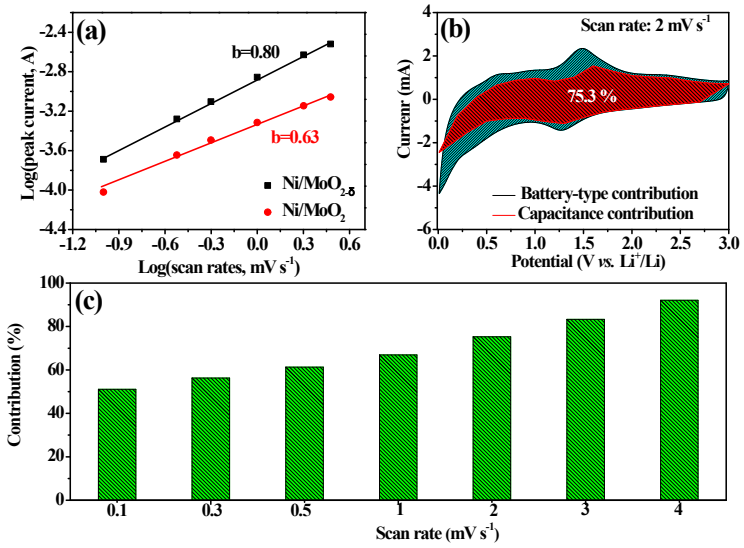

Fig. S6 (a) Current response *vs.* the scan rate for Ni/$MoO_{2-\delta}$ and Ni/MoO_2. (b) The capacitive contribution to charge storage of Ni/$MoO_{2-\delta}$ at 2 mV s^{-1}. (c) The percentage of capacitance contribution of Ni/$MoO_{2-\delta}$ at different scan rates.

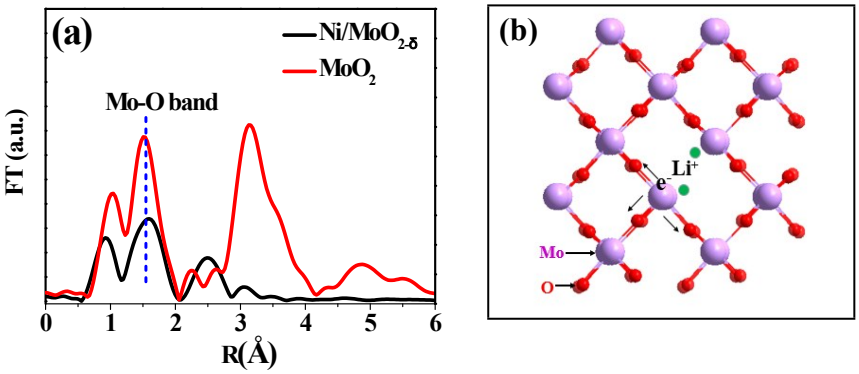

Fig. S7 (a) Fourier transform k^3-weighted EXAFS spectra of Ni/$MoO_{2-\delta}$ and MoO_2. (b) The proposed lithium storage mechanism of $MoO_{2-\delta}$ around the oxygen vacancy region.

Fig. S7a shows the Fourier-transformed k^3-weighted EXAFS spectra, and the peak at around 1.55 Å observed in both samples can be assigned to the representative Mo-O bond. Clearly, this peak for Ni/$MoO_{2-\delta}$ is obviously weaker than that for the bare MoO_2, indicating that the coordination number of Mo-O decreases, and meanwhile, the disorder degree significantly increases. The decreased Mo-O coordination can lead to many Mo dangling bonds (unoccupied electron) around the oxygen vacancy region, which can act as extra active sites to harvest the lithium species *via* electrostatic attraction (**Fig. S7b**).

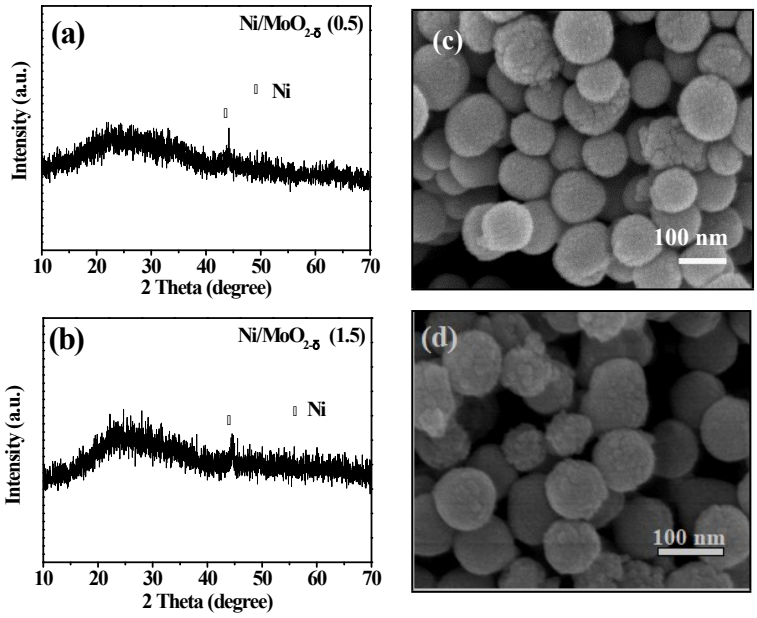

Fig. S8 XRD patterns and FESEM images of Ni/$MoO_{2-\delta}$-1 (a,c) and Ni/$MoO_{2-\delta}$-2 (b,d).

Table S1 the molar ratios of Ni/Mo in series Ni/$MoO_{2-\delta}$ samples by ICP-MS.

Samples	Molar ratio of Ni/Mo
Ni/$MoO_{2-\delta}$ -1(0.5)	1:7.32
Ni/$MoO_{2-\delta}$ (1.0)	1:5.23
Ni/$MoO_{2-\delta}$ -2(1.5)	1:4.15

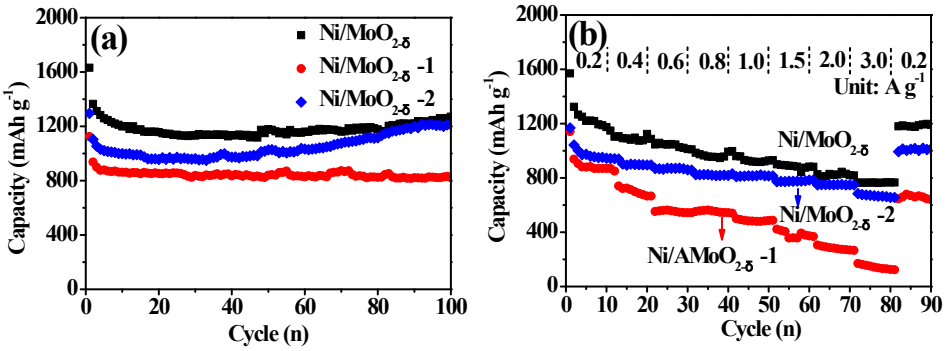

Fig. S9 (a) Cycling performances tested at the current density of 0.2 A g^{-1} and (b) rate performances of Ni/$MoO_{2-\delta}$-1, Ni/$MoO_{2-\delta}$, and Ni/$MoO_{2-\delta}$-2.

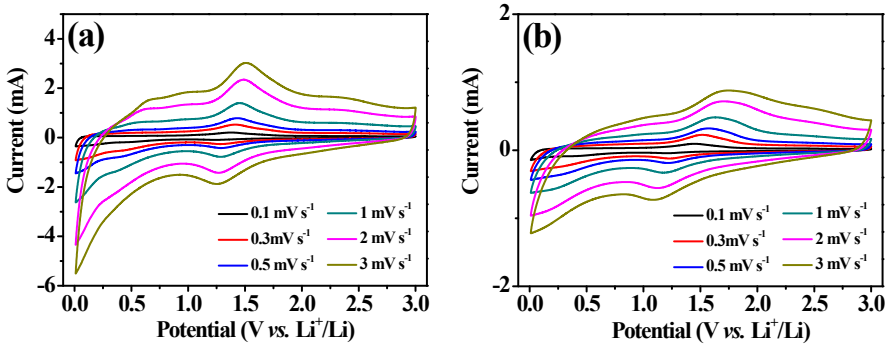

Fig. S10 CVs of Ni/$MoO_{2-\delta}$ (a) and Ni/MoO_2 (b) at different scan rates.

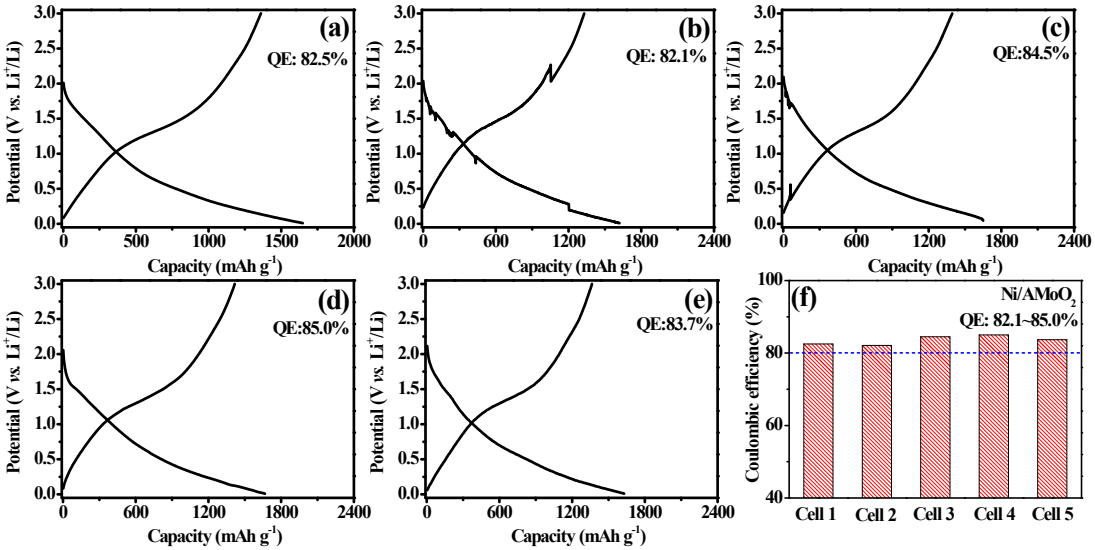

Fig. S11 The first discharge/charge voltage profiles (a-e) and initial Coulombic efficiencies (f) for five different cells based on Ni/$MoO_{2-\delta}$ at a rate of 0.2 A g^{-1}.

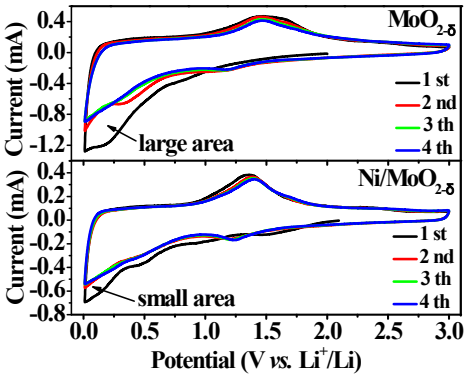

Fig. S12 CV curves of Ni/$MoO_{2-\delta}$ and $MoO_{2-\delta}$.